Doi: 10.31276/VJSTE.61(4).14-28

The 50 cm telescope of Hoa Lac observatory: an introduction

Nguyen Thi Thao[1, 2*], Mai Thuy Dung[1], Pham Vu Loc[1], Nguyen Thi Kim Ha[1], Pham Ngoc Diep[1], and Pierre Darriulat[1]

[1]Department of Astrophysics, Vietnam National Space Center, Vietnam Academy of Science and Technology
[2]Graduate University of Science and Technology, Vietnam Academy of Science and Technology

Received 20 September 2019; accepted 12 November 2019

Abstract:

The Vietnam National Space Center has recently established an observatory in Hoa Lac, near Ha Noi. The observatory is equipped with a 50 cm diameter Ritchey-Chrétien optical telescope. The authors report on first measurements illustrating its performance and demonstrate its excellence as a training tool for university students at bachelor's and master's degree levels.

Keywords: **astronomy, CCD camera, telescope.**

Classification number: **2.1**

1. Description of the telescope

The Hoa Lac observatory (105º 32'' 31'' E, 21º 01' 07'' N, near sea level) of the Vietnam National Space Center (VNSC) was commissioned in June 2018. It hosts a 50 cm (f/8) Ritchey-Chrétien reflecting telescope [1] equipped with a CCD array in the focal plane. Fig. 1 displays photographs of the observatory and of the telescope. A similar telescope equips the Nha Trang VNSC observatory in Hon Chong. Here, we report on measurements illustrating the performance of the former.

1.1. Optics

The telescope is of the Ritchey-Chrétien type, a variant of the Cassegrain design. It includes a primary mirror which reflects the light onto a smaller coaxial secondary mirror. The secondary mirror produces the image on the focal plane located behind the primary mirror and then the light beam passes through the small central hole of the primary mirror (Fig. 2). The Ritchey-Chrétien design uses hyperbolic mirrors aimed at suppressing off-axis optical errors such as coma and spherical aberration, but it introduces some

Fig. 1. Left: the Hoa Lac observatory telescope, installed in the dome and equipped with field rotator and camera. Right: the Hoa Lac observatory with the telescope dome in the foreground.

*Corresponding author: Email: ntthao02@vnsc.org.vn

astigmatism. Each mirror has a nominal reflectivity of 96% and a wave-front peak-to-valley precision of a fifth of a wavelength at λ=632 nm. Small diffraction spikes caused by light diffracting around the support vanes of the secondary mirror are present on images of bright sources. The focal length, nominally 4 m, can be finely adjusted by shifting the secondary mirror along its axis.

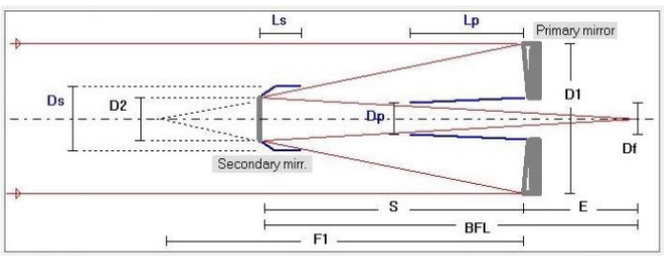

Fig. 2. Schematic of the telescope optics. The main dimensions are as follows: primary curvature radius=3500 mm; secondary curvature radius=2294 mm; primary to secondary distance=1105 mm; secondary mirror diameter (D_2)=200 mm, magnification=2286, back focal length=1475 mm; linear obstruction=48%; aperture ratio=8; light-shield length (L_s=128 mm and L_p=588 mm); light shield diameter (D_s=240 mm and D_p=150 mm); effective focal length=4 m; primary focal length (F_1^p)=1750 mm; primary diameter (D_1)=500 mm; distance between the primary mirror and the focal plane (E)=370 mm; field diameter (D_f)=50 mm.

1.2. Drive

The telescope mount is of the altitude-azimuth (altazimuth) type. The image of the environment of a star to which the telescope is pointing rotates in the image plane as the star is moving. The rotation of the image is maximal when pointing to the north pole (i.e. 90^0 declination). It is compensated by having the CCD array of the camera on a rotating support, called the field rotator. However, in the present work, the field rotator has not been used. The telescope can be driven on tracking mode for exposure times exceeding a fraction of a second. For example, near the equator, when the telescope points to a fixed direction, the field of view is typically covered in a time of only 2 minutes, or about 30 ms per pixel.

1.3. Camera

The CCD camera (Finger Lakes Instrumentation, PL16801) [2] uses a 4096×4096 pixel array with an individual pixel size of 9×9 μm^2. Each pixel covers an angle of 0.46×0.46 arcsec^2, meaning it has a field of view of 31.7×31.7 arcmin^2. The quantum efficiency exceeds 50% and peaks between 600 and 700 nm, as displayed in Fig. 3. Peltier elements cool the array to the required temperature, however, not lower than ~50^0 below ambient. Read-out proceeds at 8 MHz, meaning in practice a read-out time of 4 s per frame. However, the read-out time can be decreased by grouping together neighbouring pixels or selecting a sub-frame, with both options being available by software. Saturation occurs at a level of 10^5 electron units (eu). The signal is sampled by a 16-bit analog-to-digital converter (ADC), each ADC unit (ADCu) being equal to 1.7 eu.

Hysteresis in the CCD array, producing so-called residual bulk images (RBI), is caused by the presence of saturated pixels from the preceding exposure. It can be eliminated by illuminating the array with a ring of light emitting diodes before exposure, a procedure known as RBI pre-flood, which is also available by software. However, this technique has not been used in the present work.

1.4. Monitoring and control

A flow chart of the monitoring and control operation is displayed in the right panel of Fig. 3. It uses the Sky X Pro software [3] to streamline various tasks, which are, in turn, handled by other software, such as Maestro [4] for the telescope movements. A detailed description of the available tasks is beyond the scope of the present introduction. However, it is sufficient to mention that the movements of the telescope and dome are coupled and can be adjusted either in fixed or tracking mode. The pointing direction can be specified either by its horizontal coordinates or by its equatorial coordinates. Each picture is accompanied by a header that summarizes data of relevance, such as latitude, longitude, equatorial and horizontal coordinates of the CCD centre, calendar date, universal time, local sidereal time and local hour angle, exposure time, position of the secondary mirror, and CCD temperature.

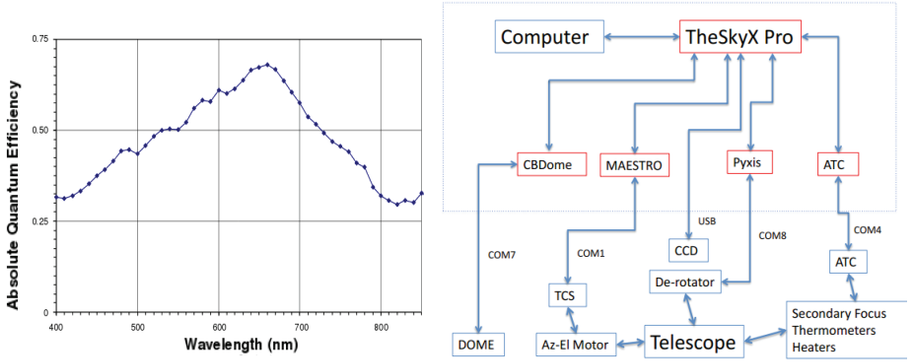

Fig. 3. Left: wavelength dependence of the quantum efficiency of the CCD array. Right: flow chart of the monitoring and control tasks.

2. The CCD camera: bias frames, dark frames and flat field frames

Basic properties of the CCD array and of the telescope optics have been measured by recording reference images referred to as bias frames, dark frames, and flat field frames. They are needed for a proper interpretation of the telescope images. The present section describes and analyses the associated data.

2.1. Bias frames and dark frames

Bias frames and dark frames are recorded with no light reaching the CCD array, the CCD shutter being closed and the telescope cap in position. The frames are recorded at different exposure times, t, during which charge is allowed to accumulate in the CCD pixels. A dark frame having zero exposure time, or more precisely, the minimum possible exposure time of 1 ms, is called a bias frame. This appellation refers to a common bias that is applied to each pixel in order to guarantee that all measured charges are well above zero and within the range of the ADC (16 bits, 65536 ADCu). The bias has been adjusted to produce a charge of approximately 1000 ADC units (ADCu). We refer to this bias as the pedestal.

2.1.1. Thermal noise, dark current and read-out noise:

The distribution of the charges measured in each of the $(4096)^2$ pixels is observed to be Gaussian to an excellent precision and nearly constant from frame to frame with a common standard deviation of some 10 ADCu. Table 1 and Figs. 4 to 6 summarize measurements of bias and dark frames for a number of combinations of exposure time, t, and temperature, T.

A typical distribution of pixel charges is shown in Fig. 4 (left). A Gaussian fit to the charge distribution gives a mean value of Q_0 +1000 ADCu with a standard deviation of σ_0 ADCu. Table 1 lists values of Q_0 and σ_0 for different combinations of temperature and exposure time. The Gaussian fit describes the measured distribution down to ppm level on the low charge side, which is remarkable, but reveals the presence of an excess of high charges. We measure the importance of this high charge tail as the ratio R_{hi} between the number of pixels having a charge larger than $Q_0+5\sigma_0$ and a charge smaller than $Q_0+5\sigma_0$.

The dispersion of the pixel charge distribution depends only slightly on temperature and exposure time; the smallest and largest values of σ_0 listed in Table 1 differ by less than 1 ADCu. On the contrary, Q_0 displays a small linear increase with exposure time as illustrated in Fig. 4 (right) and an exponential increase with temperature; it is well described by a form Q_0=-1.3+7.40 (1+0.0112 t) exp(0.112 T), where Q_0 is in units of ADCu, t in s, and T in ^{0}C. Both thermal noise, associated with the dark current thermally generated in the CCD array, and read-out noise, associated with the noise inherent to the read-out amplifier preceding the ADC, contribute to Q_0 and σ_0. The exponential temperature dependence with a characteristic temperature of around 10^0 is typical of silicon devices. Indeed, the dependence on temperature of the dark current [5] takes the form exp(-$\Delta E/kT$) where ΔE is the activation energy and k Boltzmann constant. Developing this expression about the mean temperature, T_0, we obtain, to first order in the temperature span, a dependence of the form exp($\Delta E \times T/kT_0^2$), which for T_0=270K gives ΔE=0.112kT_0^2=0.7 eV, consistent with expectation. The low value of σ_0, equivalent to 15 to 20 electrons, demonstrates the high quality of the CCD array. When adding the charges of n pixels, the relative contribution of the noise decreases as $1/\sqrt{n}$ as long as n does not exceed 1000 or so; however, for larger pixel samples, other contributions to the noise prevent further decrease.

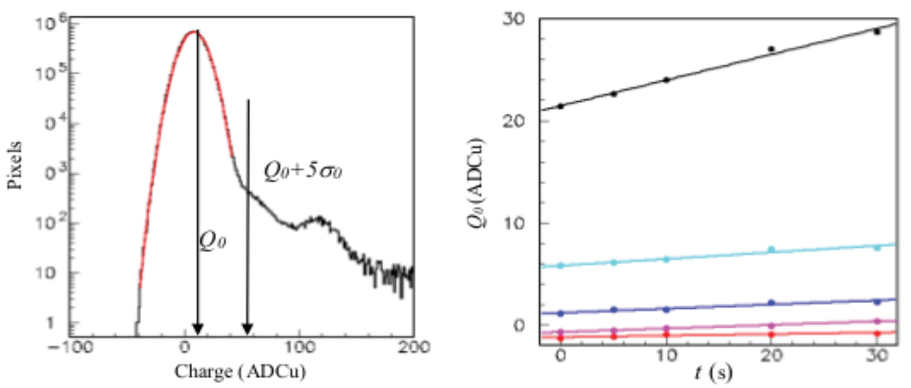

Fig. 4. A typical dark frame (t=20 s and T=0°C). Left: distribution of the pixel charges (in excess of a nominal pedestal of 1000 ADCu). The bin size is 1 ADCu. The red curve is a Gaussian fit having mean Q_0 and rms σ_0. The arrows show the value of Q_0 and of $Q_0+5\sigma_0$, the latter being used to measure the value of R_{hi} (see text). Right: dependence of Q_0 on temperature, T, and exposure time, t (s in abscissa). Colours are red, purple, blue, magenta and black for T=-25°C, -20°C, -10°C, 0°C, and 10°C, respectively.

2.1.2. Non-uniformity of the charge distribution on the pixel array:

We use coordinates x and y on the pixel array, measured in pixel size (1 px=9 μm). Read-out proceeds by shifting charges downward (decreasing y) in columns of increasing x; namely the first pixel read-out is (x, y)=(4096, 1), followed by (4096, 2) and so on up to (4096, 4096) for the last column; then we have (4095, 1)… (4095, 4096)… (1, 1)… (1, 4096). The distribution of charges on the CCD array is illustrated in Fig. 5 (left) and is observed to be non-uniform. Such non-uniformity is known to be present in all CCD arrays and is largely due to contaminations in the fabrication process. In particular, in the present case, pixel columns having x<~300 contain higher charges and, among these, pixels with y<300 contain even higher charges (Fig. 5 right). We measure this lack of uniformity with two numbers, Δ_x and Δ_{xy}. Δ_x is the difference between the mean pixel charge in pixel columns having x≤300 and pixel columns having x>300; Δ_{xy} is the difference between the mean charges contained in pixels having x≤300 and y≤300 and those contained in pixels having x≤300 and y>300. Table 1 shows that both Δ_x and Δ_{xy} are nearly independent of temperature and exposure time, with the exception of Δ_{xy}, nearly cancelling for bias frames. On average, over all measurements listed in Table 1, Δ_x=1.15±0.12 ADCu and Δ_{xy}=3.35±0.18 ADCu for dark frames, and Δ_{xy}=0.2±0.1 ADCu for bias frames. It is therefore sufficient to look at the dark frame having the lowest values of temperature and exposure time, -25^{0}C and 5 s respectively, to see the effect of the non-uniformity of the pixel charge distribution over the CCD array. This is illustrated in Fig. 6 that displays projections of the charge map over the x and y axes, both over the full range of 4096×4096 px^2 and over the restricted environment of the (x, y)=(0, 0) corner of the array, of size 300×300 px^2. The enhancements at low x and y values are described by exponentials having amplitudes of 17 ADCu in x and 10 ADCu in y with decay lengths of 67 pixels in x and 103 pixels in y.

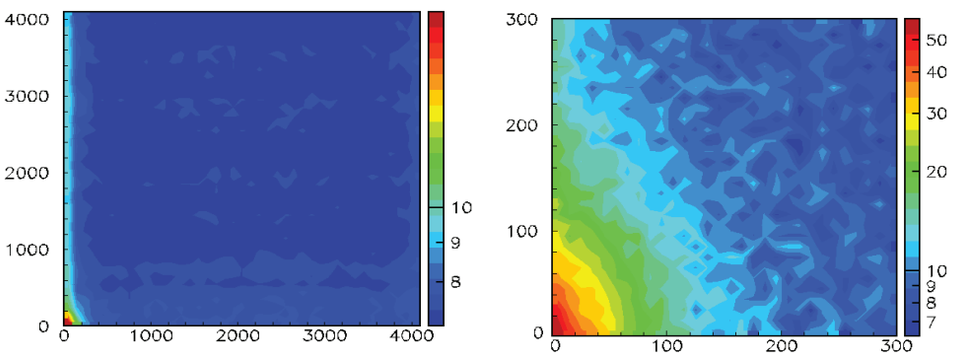

Fig. 5. A typical dark frame (t=20 s and T=0^{0}C). Left: map of the pixel charges (in excess of a nominal pedestal of 1000 ADCu) not exceeding $Q_0+5\sigma_0$. Each (x, y) bin of the map is averaged over 100×100 pixels. Right: zooming on the left panel close to the lower-left corner of the CCD array (x=y=0). Each (x, y) bin of the map is now averaged over 10×10 pixels.

Table 1. Bias and dark frames. Summary of results obtained for different values of the temperature (T) and of the exposure time (t).

T (^{0}C)	t (s)	Q_0 (ADCu)	σ_0 (ADCu)	R_{hit}	Δ_x (ADCu)	Δ_{xy} (ADCu)
-25	0	-1.3	9.46	6.0 10^{-7}	0.9	0.3
	5	-1.1	9.47	2.3 10^{-5}	1.1	3.1
	10	-0.9	9.47	3.5 10^{-5}	1.1	3.4
	20	-0.9	9.48	5.9 10^{-5}	1.1	3.6
	30	-0.8	9.48	7.5 10^{-5}	1.1	3.6
-20	0	-0.7	9.47	9.5 10^{-7}	0.9	0.3
	5	-0.5	9.48	3.2 10^{-5}	1.1	3.1
	10	-0.3	9.48	4.5 10^{-5}	1.1	3.4
	20	-0.1	9.49	7.8 10^{-5}	1.2	3.4
	30	0.4	9.50	1.1 10^{-4}	1.1	3.6
-10	0	1.	9.52	2.1 10^{-6}	0.9	0.0
	5	1.1	9.53	5.1 10^{-5}	1.2	3.2
	10	1.5	9.54	9.4 10^{-5}	1.2	3.4
	20	2.2	9.55	2.0 10^{-4}	1.2	3.4
	30	2.3	9.56	4.0 10^{-4}	1.2	3.5
0	0	5.8	9.65	2.1 10^{-6}	1.0	0.2
	5	6.1	9.67	1.2 10^{-4}	1.2	3.2
	10	6.4	9.68	3.4 10^{-4}	1.3	3.2
	20	7.4	9.71	8.5 10^{-4}	1.3	3.5
	30	7.6	9.73	1.3 10^{-3}	1.3	3.4
10	0	21.4	10.07	4.7 10^{-6}	1.1	0.2
	5	22.6	10.10	4.8 10^{-4}	1.3	3.0
	10	24.0	10.20	1.0 10^{-3}	1.3	3.2
	20	27.0	10.30	1.8 10^{-3}	1.3	3.2
	30	28.7	10.41	2.5 10^{-3}	1.3	3.6

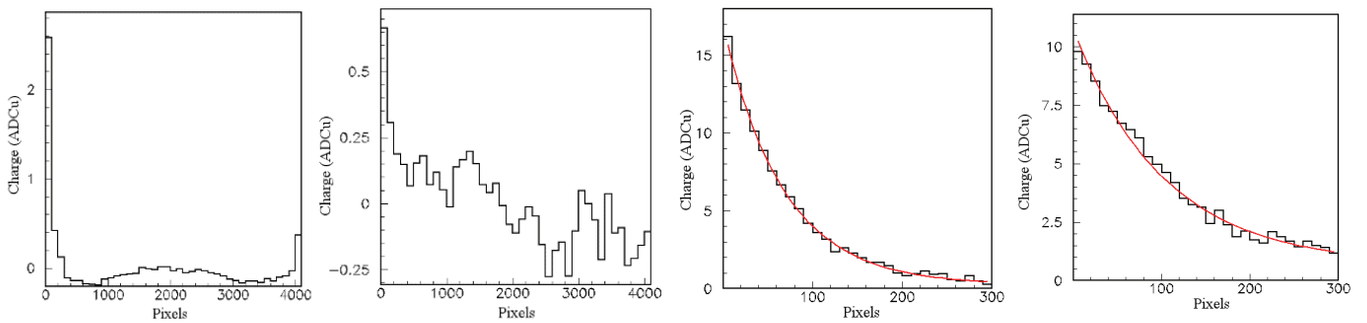

Fig. 6. Dark frame having *t*=5 s and *T*=-25^{0}C. Projections on the *x* (left) and *y* (middle-left) axes of the whole charge map (pedestal subtracted). Middle-right and right: same as the left panels for the 300×300 pixels^2 lower-left square of the CCD array. Curves are exponential fits (see text).

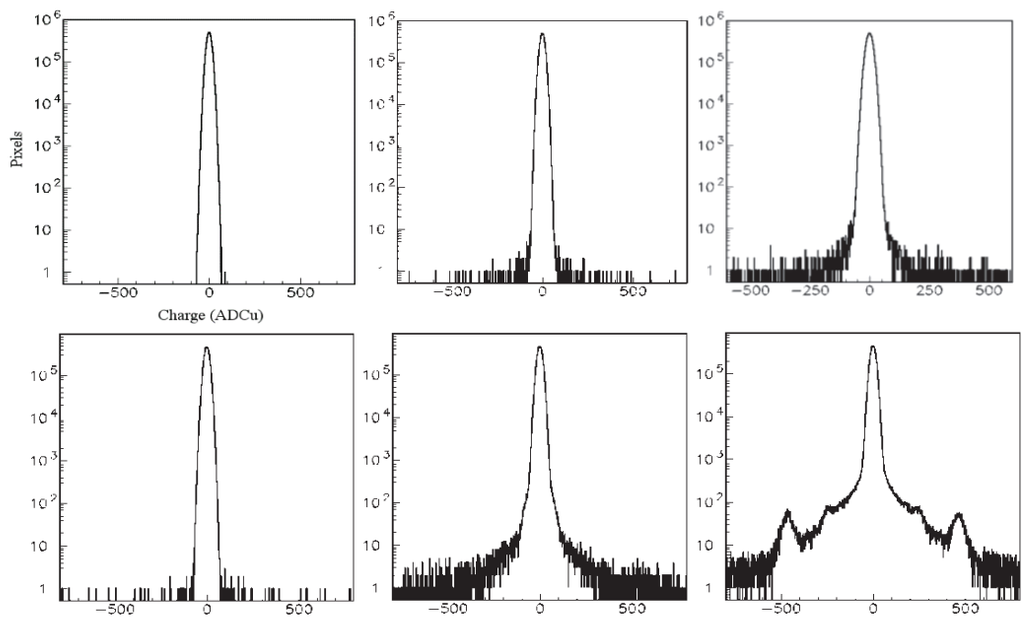

Fig. 7. Warm pixels. Distributions of the difference between the charges (ADCu) contained in two adjacent pixels (having *y* values differing by one unit and the same value of *x*). Upper panels: *T*=-25^{0}C; lower panels: *T*=10^{0}C; left panels: bias frames; central panels: *t*=5 s; right panels: *t*=30 s.

2.1.3. Warm pixels:

In the preceding section, we studied pixels having a content not exceeding a typical value of $Q_0+5\sigma_0$. However, the maps of pixels having larger charges display isolated points associated with what is called warm pixels, due to charge leakages across the CCD array caused by contamination during production. Warm pixels are easily identified as containing a charge much higher than their immediate neighbours in the array. Fig. 7 and Table 2 display distributions of the difference between the charges contained in two adjacent pixels for various combinations of exposure time and temperature. Warm pixels are seen to populate wings of these distributions having amplitudes that depend on both temperature and exposure time. To a very good approximation, their amplitude is proportional to exposure time; the proportionality factor R_{hot} is listed in the last column of Table 2; its distribution as a function of temperature is shown in Fig. 8 (left); it increases exponentially as 20 exp(0.09 *T*) (s^{-1}) with again a characteristic temperature of around 10^0.

Table 2. Number of pairs of adjacent pixels containing charges differing by more than 1000 ADCu.

	0	5 s	10 s	20 s	30 s	R_{hot} (s^{-1})	$20e^{0.09T}$
-25^{0}C	0	13	19	42	62	2.2	2.1
-20^{0}C	0	17	31	68	108	3.4	3.3
-10^{0}C	0	39	90	192	268	8.8	8.1
0^{0}C	0	100	219	414	615	20.8	20.0
10^{0}C	1	253	525	1021	1521	51.2	49.2

However, the shape of the distribution of the charges contained in warm pixels is independent of temperature and exposure time; as illustrated in Fig. 8 (right) it decreases exponentially with a common characteristic charge of between 800 and 900 ADCu. When a pixel is warm in a given combination of temperature and exposure time, it is also warm in any other combination having either a larger temperature or a larger exposure time (or both): being warm is a property of the pixel, which justifies the denomination.

Fig. 9 displays the dependence of R_{hi} (defined in Section 2.1.1 and listed in Table 1) on exposure time and temperature. It increases exponentially with temperature, approximately as R_{hi}=3.5 10^{-5} exp(0.08 T) $t^{1+0.008T}$, again displaying a characteristic temperature at the scale of 10^0. The question then arises of the relation between the tail of the charge distribution measured by R_{hi} and warm pixels. We answer it in the typical case of the (t=20 s, T=0^{0}C) dark frame illustrated in Fig. 4. We consider charges Q in the tail of the distribution (Q>1047 ADCu) and study the correlation between Q-1007 ADCu (defining tail charges) and Q- $Q_{neighbour}$ (defining warm pixels, $Q_{neighbour}$ being the charge of the adjacent pixel in the read-out sequence). Fig. 9 (middle and right) shows that essentially all tail charges are from warm pixels, namely are isolated.

The bumps seen at ~120 ADCu in Fig. 4 and at ~240 ADCu and ~480 ADCu in the lower right panel of Fig. 7 represent a small fraction of the warm pixel population. They are uniformly distributed over the CCD array and are only present for temperatures equal to or larger than 0^{0}C. In contrast with other warm pixels that display a temperature-independent and exponentially decreasing charge distribution, their charges cluster about values that depend on exposure time and temperature. We fail to understand what causes their presence.

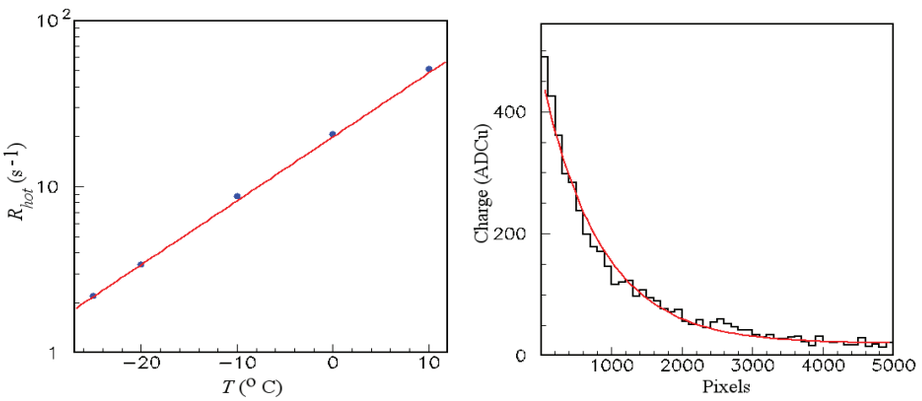

Fig. 8. Warm pixels. Left: dependence of R_{hot} (s^{-1}) on temperature T (^{0}C). Right: charge distribution of hot pixels (in excess of the charge of the adjacent pixel charge increased by 1000 ADCu). The curve is an exponential fit of the form exp(-Q/841).

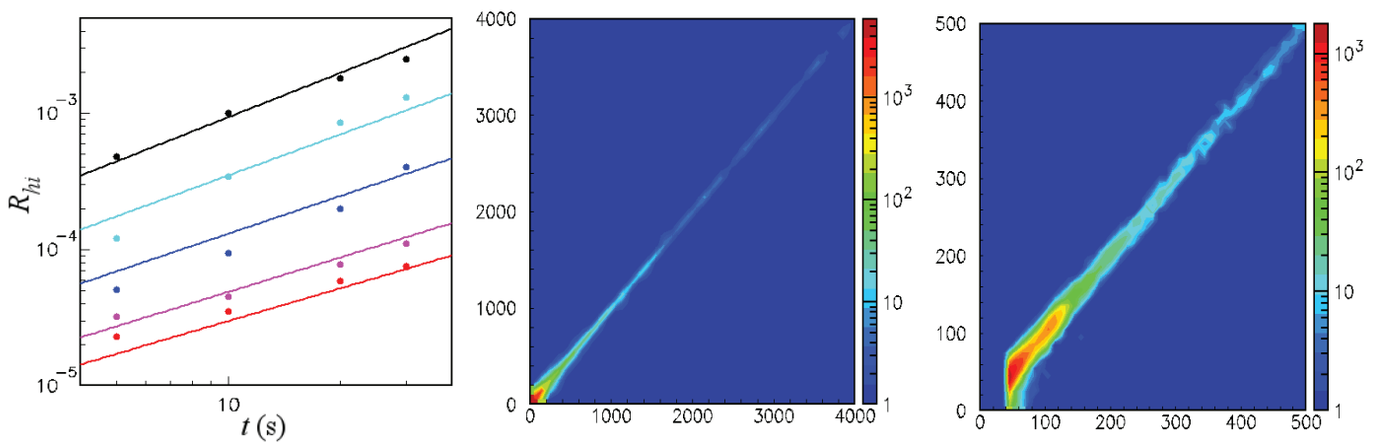

Fig. 9. Warm pixels. Left: dependence of R_{hi} (ordinate) on t (s, abscissa) for different values of the temperature: -25^{0}C (red), -20^{0}C (purple), -10^{0}C (blue), 0^{0}C (magenta) and 10^{0}C (black); the curves are fits of the form R_{hi}=3.5 10^{-5} exp(0.08 T) $t^{1+0.008\ T}$. Middle and right: (t=20 s, T=0^{0}C) dark frame; correlation between tail charges Q and warm pixels. The abscissa is Q-1007 ADCu for Q>1047 ADCu and the ordinate is Q-$Q_{neighbour}$. The right panel is a zoom of the middle panel at lower Q values.

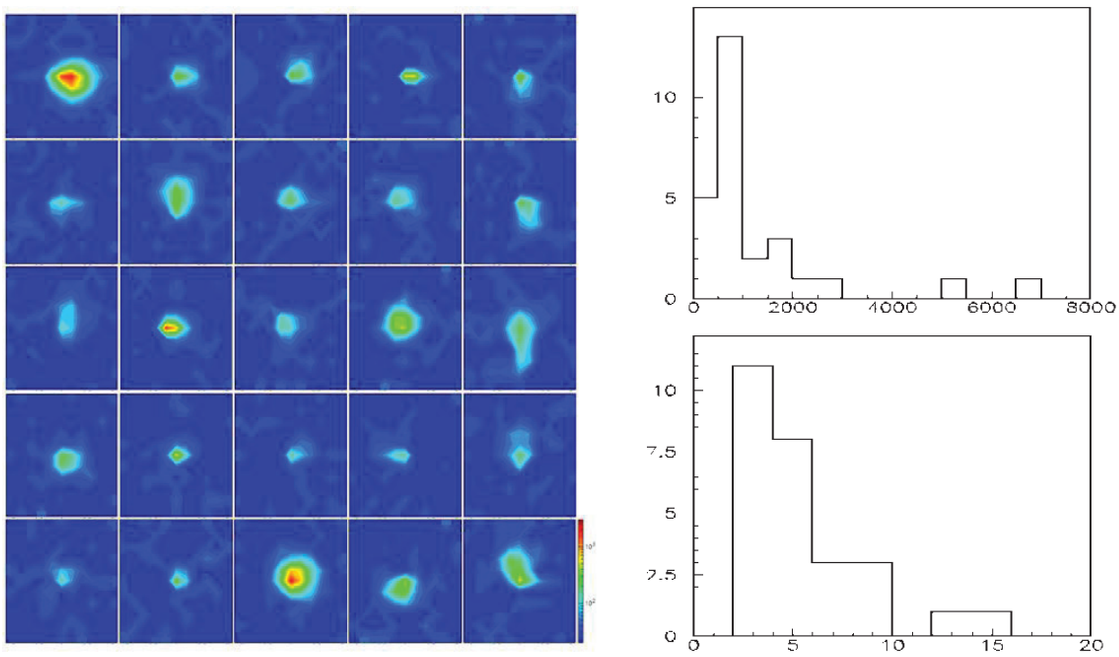

Fig. 10. Cosmic rays. Left: charge maps of 25 of the 27 recorded cosmic ray impacts (see text). Each map is 11×11 px^2, namely 0.1×0.1 mm^2 in area. A common colour scale (ADCu) is used for all maps (shown in the lower right corner). Right: distribution of the charges (ADCu, upper panel) and of the number of pixels hit (lower panel) for the 27 detected cosmic ray impacts.

2.1.4. Cosmic rays:

We expect cosmic rays to cross the ~14 cm^2 of the CCD array at a rate of approximately one every 4 s [6, 7]. In order to detect a significant sample, we record 25 bias frames at T=-25^{0}C and select pixel charges exceeding Q_0+8σ_0. We find five warm pixels, easily identified by their isolation, generally present in several frames (respectively 8, 7, 5, 2 and 1) and 27 clusters of a few pixels that are associated with cosmic ray impacts on the CCD array. Their number is consistent with the time during which the array is sensitive, slightly more than half the read-out time on average. Their maps are displayed in Fig. 10 (left) and the distribution of their charges (~1400 ADCu on average) and of the number of pixels in the cluster (~6 on average) in Fig. 10 (right). These values conform with expectation; minimum ionizing muons lose some 1.8 MeV per g/cm^2 of silicon, meaning ~400 eV/μm for a silicon density of 2.3 g/cm^3. The average 1400 ADCu (~2400 electrons) correspond, therefore, for a production of an electron per 3.6 eV, to a track length of ~20 µm, namely a depleted sensitive layer thickness at the ~10 µm scale.

2.2. Flat field frames

In addition to the non-uniformity of the charge distribution measured in bias and dark frames that has been revealed in the preceding sections, vignetting can be expected to cause the response of a pixel to a given photon flux to depend on its location in the array. Vignetting occurs when light reflected by the primary mirror misses the secondary mirror; it is more important for sources that are farther off axis and results in a loss of illumination that increases with the distance, r, of the pixel from the centre of the array.

Flat field frames were recorded in November 2018 at twilight pointing to altitudes for which the sky brightness was reasonably uniform over the field of view, and to azimuths opposite to the setting Sun, with an illumination of typically half saturation. As an illustration of the main features, measurements made on a flat field frame recorded at T=0^{0}C and t=20 s are displayed in Fig. 11 after a pixel-by-pixel subtraction of the dark frame taken under the same conditions of temperature and exposure time. The subtracted charge, ΔQ, peaks above an irregular background. We characterize its profile by the mean $<\Delta Q>$ and the standard deviation, σ_q, of a Gaussian fit to the peak. Here, $<\Delta Q>$=40430 ADCu and σ_q=370 ADCu. We measure the importance of the background by the deviation from unity of the ratio, R, between the charge contained within 5σ_q of $<\Delta Q>$ and the total charge summed over the whole

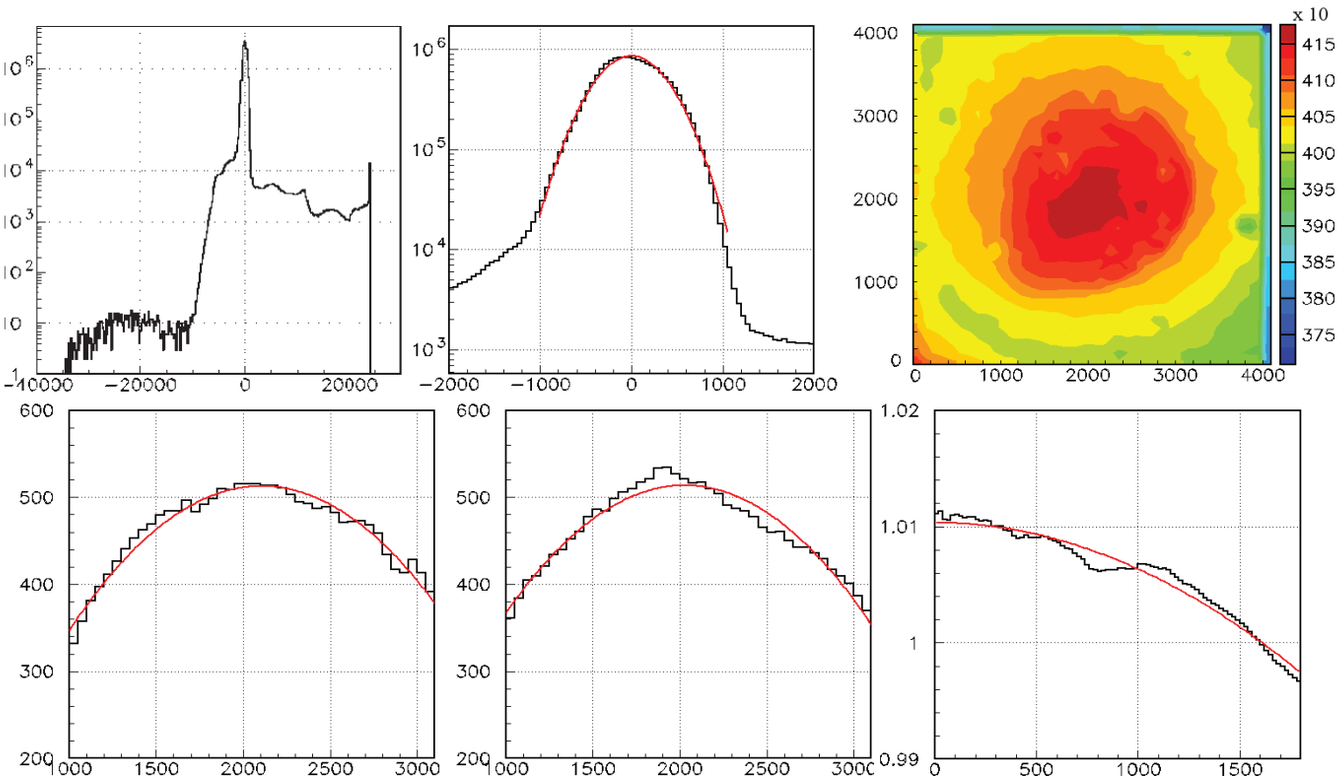

Fig. 11. Flat field frame (dark frame subtracted) recorded at (T=0^{0}C, t=20 s). Upper-left and upper-middle panels: charge distribution after subtraction of $<\Delta Q>$, the middle panel being a zoom of the left panel about the origin. The curve in the upper-middle panel is a Gaussian fit. Upper-right panel: distribution of the mean charge per pixel (there are 100×100 pixels in each bin of the histogram, the colour scale is in units of 100 ADCu). Lower-left and lower-middle panels: projections on the x and respectively y axes of the central square of the charge, with both x and y contained in the interval [1000, 31000] px; a constant charge has been subtracted from ΔQ and the curves are parabolic fits used to measure $<x>$ and $<y>$. Lower-right panel: dependence of $R=\Delta Q/<\Delta Q>$ on r for r<1800 px; the red curve is a fit of the form $R/R_0=1-\lambda(r/1000)^2$.

array. Here, $1-R_q$=7.4%, which is two orders of magnitude larger than the corresponding value of R_{hi} (8.5 10^{-4}) listed in Table 1. The distribution of ΔQ over the CCD array is shown in the upper-right panel of Fig. 11. Using a colour scale confined to a narrow window centred on$<\Delta Q>$ reveals very clearly a central enhancement, spanning some 5% of the central value from centre to edge. The illumination is seen to be slightly off-centre. We evaluate the coordinates ($<x>$,$<y>$) of its centre by making parabolic fits of the projection on the x- and y- axes of the charge distribution of the central 2100×2100 px^2 of the array, where $<x>$=2104 px and $<y>$=2026 px. We define r in each pixel, (x, y), as $r=[(x-<x>)^2+(y-<y>)^2]^{½}$. The dependence of $\Delta Q/<\Delta Q>$ on r is then fitted to the central disc r <1800 px to the form $R=R_0[1-\lambda(r/1000)^2]$. If the non-uniform illumination were due to vignetting, we would expect the values of $<x>$, $<y>$, and λ to be independent of the values of T and t. However, this is not at all the case.

The flat field frames recorded at temperatures below 0^{0}C are found to behave very differently from those recorded at positive temperatures. As will become apparent from what follows, the reason is the presence of ice between the CCD array and the glass window that covers it, forming a pattern of very small droplets acting as lenses in front of the pixels.

Indeed, visual inspection of the CCD array at temperatures below 0^{0}C reveals the presence of frozen condensation. Such a pattern is shown in Fig. 12 for a small but typical region of the flat field frame recorded at T=-25^{0}C and t=30 s; also shown on the figure is the charge distribution recorded over the whole array, with values of $<Q>$= 20989 ADCu, σ_q=254 ADCu and $1-R_q$=0.198, compared with R_{hi}=7.5 10^{-5} for the corresponding dark frame (Table 1). A small cluster of some 20 pixels is observed to surround the largest charge pixel associated with each water droplet. This is illustrated in the right panel of Fig. 12, which displays

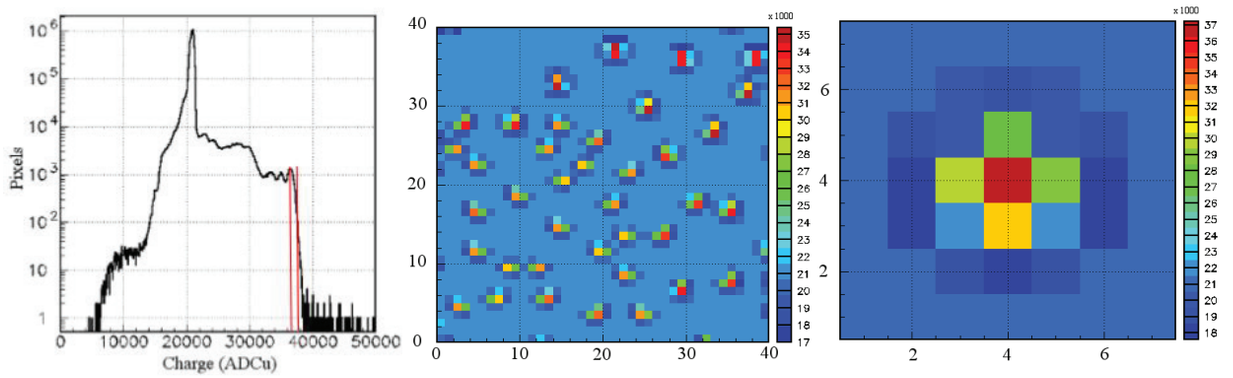

Fig. 12. Flat field frame recorded at (*T*, *t*)=(-25^{0}C, 30 s). Left panel: charge distribution (ADCu). Middle panel: typical pattern as observed in the small square of the CCD array defined as 1500<*x*<1540 px and 3000<*y*<3040 px. Right panel: charge pattern averaged over 4966 squares of 7×7 px^2, centred on a pixel selected for having a charge between 37000 and 38000 ADCu (between the red lines shown on the left panel).

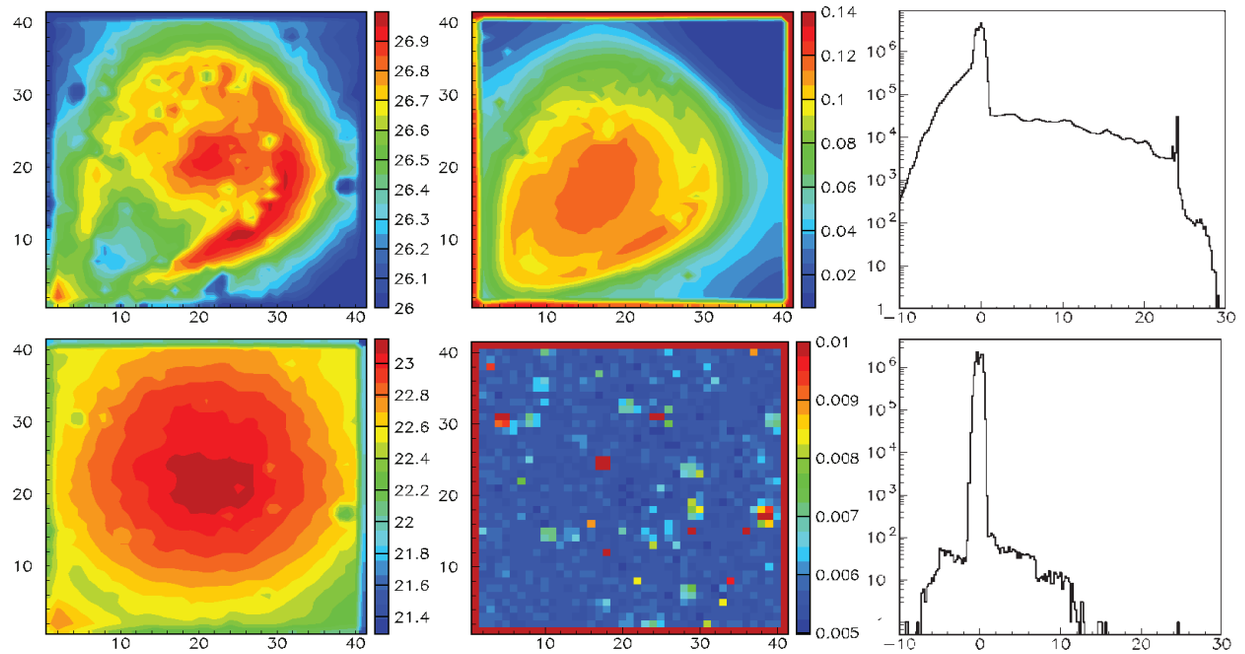

Fig. 13. Flat field frames averaged over 12 frames recorded at *T*=-25^{0}C, -20^{0}C and -10^{0}C for *t*=5, 10, 20 and 30 s (upper panels) and over 3 frames recorded at *T*=10^{0}C for 10, 20 and 30 s (lower panels). The left panels show the maps of $\langle \Delta Q \rangle_{sub}$ (*x* and *y* in units of 100 px, colour scale in units of 1000 ADCu), the middle panels the map of $\sigma_{sub}/\langle \Delta Q \rangle_{sub}$ and the right panels the charge distribution ($\langle \Delta Q \rangle$ subtracted).

the cluster shape averaged over some 5000 cases of high charge pixels (37000<*Q*<38000 ADCu) and centred on that pixel. Interestingly, it reveals the presence of a ring of charges lower than average at a distance of some 20 μm from the central pixel, approximately compensating for the central excess and supporting the interpretation in terms of a lensing effect of ice droplets.

The observed pattern of droplets is invariant for successive frames taken without warming up the CCD array to positive temperatures, independently from the precise values of temperature and exposure time. On the contrary, when the CCD is warmed up and cooled again a different pattern is observed. This, together with the facts that the phenomenon is absent from temperature below 0^{0}C dark frames (for which the CCD array is however covered with ice) and that 1-R_q is considerably higher than R_{hi} gives

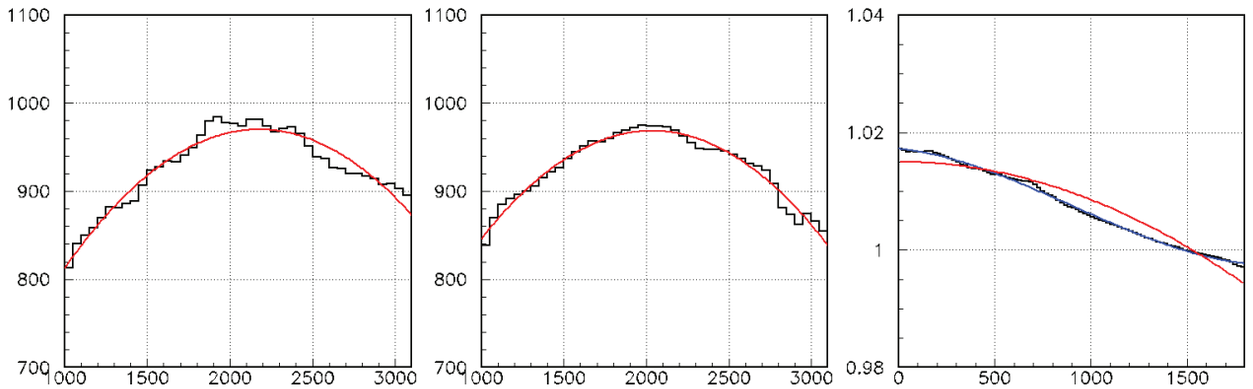

Fig. 14. Flat field frames averaged over 3 frames recorded at T=10^{0}C for 10, 20 and 30 s. The left panels show the distributions of ΔQ used to calculate $\langle x \rangle$ and $\langle y \rangle$; a constant charge has been subtracted from ΔQ and the curves are parabolic fits used to measure $\langle x \rangle$ and $\langle y \rangle$. The right panel shows the dependence on r of R/R_0. The curves show a fit of the form $R/R_0 = 1 - \lambda(r/1000)^2$ (red) and a third degree polynomial fit (blue).

evidence for the interpretation in terms of ice droplets. We illustrate this further in Fig. 13, which compares 12 flat field frames recorded at temperatures below 0^{0}C for different exposure times and 3 flat field frames recorded at 10^{0}C for t=10, 20 and 30 s. The differences are spectacular. As a measure of the effect, we calculate in each square of 100×100 pixels the mean charge $\langle \Delta Q \rangle_{sub}$ and the rms with respect to the mean σ_{sub}. The ratio $\sigma_{sub}/\langle \Delta Q \rangle_{sub}$ is found to be essentially the same for each combination of temperature below 0^{0}C and exposure time; its map is displayed in the middle panels of Fig. 13. Its shape, for temperatures below 0^{0}C, is the same as that of the frozen condensation observed visually.

The above results make it clear that negative temperature flat field frames cannot be used to evaluate the effect of vignetting. We use instead the three flat field frames recorded at T=10^{0}C with exposure times of 10, 20, and 30 s that are illustrated in the lower panels of Fig. 13. Table 3 and Fig. 14 show that they give consistent results and their dispersion is used to evaluate uncertainties. The values of $\langle x \rangle$ and $\langle y \rangle$ are measured as -14±4 px and 129±7 px, respectively, away from the centre of the array. The value of λ is (6.3±0.2) 10^{-3} but the fit is poor. A third-degree polynomial gives a much better fit with R=1.017 [1 - 0.306 10^{-2} (r/1000) - 0.124 10^{-1} (r/1000)^2 + 0.453 10^{-2} (r/1000)^3]. We retain from this analysis that the centre to edge difference of illumination due to vignetting does not exceed 3%.

Table 3. Dependence of $\Delta Q = Q_{flat} - Q_{dark}$ on the pixel coordinates x and y on the CCD array. The quantities listed are defined in the text.

T (0C)	t (s)	$\langle \Delta Q \rangle$ (ADCu)	σ_q (ADCu)	$1-R_q$ (10^{-6})	$\langle x \rangle$	$\langle y \rangle$	λ (10^{-3})
10	10	13494	144	93.4	2039	2187	6.64
	20	21112	211	70.3	2031	2171	6.29
	30	29162	274	33.9	2032	2174	6.15
Mean		-	-	-	2034	2177	6.33
RMS		-	-	-	4	7	0.21

2.3. Summary

In summary, the analysis of bias and dark frames has demonstrated the high-quality performance of the CCD array with a Gaussian charge distribution down to ppm level and a standard deviation at the level of 9 to 10 ADCu (~16 electrons). A few well-defined pixels, called warm pixels, representing a fraction of the total increasing from ppm level at -25^{0}C to permil level at 10^{0}C, deviate from the Gaussian distribution and produce a high charge tail with an exponential charge distribution typically decreasing by a factor 2 every 600 ADCu (~1000 electrons). They are distributed uniformly over the CCD array.

The thermal noise and dark current display an exponential temperature dependence consistent with a Boltzmann distribution and doubling every 6 to 8^{0}C.

The distribution of the charge is uniform over most of the CCD array, increasing only at the lower edges of the x and y

distributions (over typically 70 and 100 pixels respectively).

Cosmic rays have been detected during the exposure and read-out times, at a rate of a few tenths of Hz. They produce small clusters of 6 pixels on average carrying a mean charge of some 2000 to 3000 electrons.

The analysis of flat field frames has revealed significant water condensation behind the front glass window of the CCD array when operating at temperatures below 0^0C. In practice, we have been able to overcome this problem by keeping the CCD array in a dry atmosphere between observations, as humidity may take more than a day before building up significantly on the CCD array. The precise cause of this default, leak or outgassing, needs to be identified and corrected. The analysis of flat field frames recorded at 10^0C has revealed a small misalignment of the image on the CCD array, at millimetre level in y, and a vignetting causing a difference of illumination not exceeding 3% between centre and edge.

3. Geometry and astrometry

In order to evaluate possible misalignments of the system, reference stars have been observed with different exposure times, at different altitudes and azimuths. Here, we simply illustrate the main results by using a set of observations performed on December 17th, 2018 (Julian date JD=2458469.5).

Each picture is associated with a header that lists, among other information, the values of the calendar date, of the universal time UT and of the azimuth and altitude, az and alt, of the telescope (centre of the CCD array) as measured from the encoders of the associated movements. Knowing the equatorial coordinates of the star being observed, right ascension ra and declination dec (as obtained from the Simbad database [8], accounting for the star proper motion) and the location of the telescope on Earth (as obtained from GPS measurements and compared with values quoted by Google [9]), latitude lat=21.021^0 and longitude $long$=105.543^0, we can calculate the horizontal coordinates of the star, azimuth az_0 and altitude alt_0, using the equations below:

$$\sin(alt_0)=\sin(lat)\,\sin(dec)+\cos(lat)\cos(dec)\cos(lha)$$

$$\sin(az_0)= -\sin(lha)\cos(dec)/\cos(alt_0)$$

$$\cos(az_0)=[\sin(dec)-\sin(lat)\sin(alt_0)]/[\cos(lat)\cos(alt_0)].$$

Here, lha is the local hour angle, equal to the difference between the local sidereal time LST and the right ascension of the star, ra_0. The local sidereal time is the sum of Greenwich sidereal time, GST, and longitude, $long$. The Greenwich sidereal time is obtained from the value of universal time, UT, using the relation below (in hours):

$$GST=6.656306+0.0657098242*(JD-2445700.5)+1.0027379093*UT,$$

where JD is the Julian date [10]. Namely lha is expressed in degrees (modulo 360^0) as

$$lha=LST-ra_0=GST+long-ra_0.$$

Measuring the coordinates x and y of the star on the CCD array, we can then infer the horizontal coordinates of the centre of the CCD array, (az*,alt*) by correcting az_0 and alt_0 by the offsets (x-2048)px/cos(alt) and (y-2048)px where px=1.28^0 10^{-4} is the angular acceptance of a pixel.

Table 4 compares the values of the true horizontal coordinates of various stars at various times and the corresponding values listed in the picture headers.

Table 4. Summary of observations made on December 17th, 2018.

x (px)	y (px)	UT (hr)	az (^{0})	alt (^{0})	Δaz (^{0})	Δalt (^{0})
β Cas, ra=2.2973^0, dec=59.1488^0						
1966	1953	11.80915	356.8463	51.2952	2.1459	-0.3107
2030	2288	11.81715	356.7341	51.2438	2.1448	-0.3087
1998	2202	11.81963	356.7042	51.2533	2.1386	-0.3069
1858	1870	11.82212	356.6749	51.2963	2.1109	-0.3031
1714	2291	11.83088	356.5044	51.2440	2.0178	-0.2897
1972	1684	11.83340	356.5733	51.2982	2.1706	-0.3097
2131	1995	11.83615	356.5427	51.2509	2.2063	-0.3134
1950	2295	11.84230	356.4072	51.2177	2.1086	-0.2997
2094	2077	11.84508	356.4187	51.2319	2.1836	-0.3095
φ Aqr, ra=348.5809^0, dec=-6.0489^0						
1726	2053	11.48577	210.3983	59.3232	-0.3479	0.2809
1795	2029	11.48980	210.5243	59.2951	-0.3075	0.2786
1877	1998	11.49316	210.6336	59.2710	-0.2633	0.2747
2082	1913	11.49824	210.8210	59.2352	-0.1541	0.2647
2150	2080	11.50173	210.9094	59.1875	-0.1374	0.2636
1711	1989	11.50722	210.9593	59.1823	-0.3353	0.2867
2103	2209	11.51156	211.1424	59.1062	-0.1648	0.2703

2054	2141	11.51474	211.2222	59.0946	-0.1773	0.2733
2007	2070	11.51830	211.3129	59.0797	-0.1879	0.2754
γ Cas, ra=14.1772^0, dec=60.7167^0						
3228	2720	11.97788	4.5780	49.6847	2.5984	-0.4827
2630	2576	11.98138	4.4379	49.7334	2.3787	-0.4543
2186	2406	11.98423	4.3388	49.7759	2.2235	-0.4350
1408	1866	11.98730	4.2038	49.8803	1.9679	-0.4014
2520	1459	11.99048	4.4044	49.8721	2.4277	-0.4633
2842	2287	11.99331	4.3625	49.7626	2.4827	-0.4682
2436	2457	11.99628	4.2393	49.7658	2.3124	-0.4447
1970	2112	11.99998	4.1418	49.8315	2.1640	-0.4250
Bellatrix, ra=81.2828^0, dec=6.3497^0						
1687	2208	13.78427	103.9007	44.9081	0.6547	-1.1264
1714	2110	13.78725	103.9379	44.9592	0.6709	-1.1286
1954	1877	13.79060	104.0200	45.0149	0.7718	-1.1425
1992	1962	13.79272	104.0421	45.0384	0.7786	-1.1431
2365	2183	13.79574	104.1140	45.0352	0.8930	-1.1593
1781	2065	13.79874	104.0504	45.1201	0.6951	-1.1305
1844	2047	13.80141	104.0854	45.1560	0.7183	-1.1334
1852	2056	13.80434	104.1113	45.1960	0.7199	-1.1323
2080	1963	13.80697	104.1794	45.2314	0.8071	-1.1447
Aldebaran, ra=83.0017^0, dec=-0.2991^0						
2378	2145	13.22196	91.2207	51.6741	1.0915	-1.2121
1937	2220	13.22510	91.1490	51.7338	0.9090	-1.1869
2001	1813	13.22794	91.2102	51.8187	0.9683	-1.1939
2042	1891	13.23064	91.2254	51.8445	0.9774	-1.1961
2191	2208	13.23328	91.2410	51.8709	1.0103	-1.1661
1944	2179	13.23596	91.2112	51.8912	0.9131	-1.1872
2095	1974	13.23884	91.2730	51.9475	0.9913	-1.1976
Mintaka, ra=68.9805^0, dec=16.5084^0						
2069	2532	13.88839	112.0897	41.7553	0.6864	-1.1010
2000	2375	13.89097	112.1155	41.8112	0.6739	-1.0989
1822	1962	13.89371	112.1423	41.9032	0.6417	-1.0956
1883	1922	13.89634	112.1807	41.9375	0.6639	-1.1008
2179	2182	13.89942	112.2396	41.9321	0.7432	-1.1131
2087	2124	13.90195	112.2534	41.9752	0.7151	-1.1105
Alpheratz, ra=2.0976^0, dec=29.0896^0						
2235	2281	15.37633	292.9245	35.8846	1.4869	0.5647
1895	2279	15.37946	292.8840	35.8617	1.3876	0.5824
2343	1583	15.38277	292.9901	35.8760	1.5581	0.5509
2424	1926	15.38550	292.9770	35.7958	1.5528	0.5502
2157	2034	15.38843	292.9361	35.7587	1.4649	0.5652

We perform linear fits to the differences $\Delta az=az-az^*$ and $\Delta alt=alt-alt^*$ of the form:

$$\Delta az_{lin}=\Delta az_0+\Delta az_1\, alt+\Delta az_2\, cos(az)+\Delta az_3\, sin(az)$$

$$\Delta alt_{lin}=\Delta alt_0+\Delta alt_1\, alt+\Delta alt_2\, cos(az)+\Delta alt_3\, sin(az).$$

The distributions of the differences $\Delta az-\Delta az_{lin}$ and $\Delta alt-\Delta alt_{lin}$ are displayed in Fig. 15. Gaussian fits give standard deviations of 0.091^0 and 0.016^0 respectively. The parameters of the linear fits are listed in Table 5.

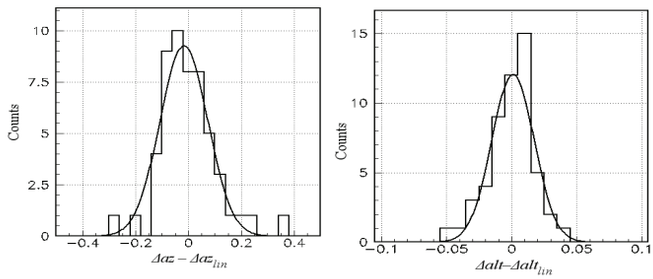

Fig. 15. Distributions of $\Delta az-\Delta az_{lin}$ (left) and $\Delta alt-\Delta alt_{lin}$ (right) as described in the text for the measurements associated with the observations listed in Table 4.

Table 5. Values of the parameters of the linear fits to $\Delta az-\Delta az_{lin}$ and $\Delta alt-\Delta alt_{lin}$.

	Δ_0	Δ_1	Δ_2	Δ_3
Azimuth	1.4580	-9.84 10^{-3}	1.2635	6.81 10^{-2}
Altitude	-0.2047	-1.56 10^{-3}	-0.1157	-0.9185

They are dominated by the dependence on az and, at a typical altitude of 50^0, they can be crudely approximated by the simpler forms

Δaz=1.0^0+1.3^{0}cos(az-3^0) and Δalt =-0.3^0-0.9^{0}sin(az+7^0).

This suggests a dominant contribution from a tilt of the telescope axis. Indeed, measuring such a tilt by the associated Euler angles φ, ψ and β and calling $\alpha=\varphi+\psi$, a rotation of (x, y, z) into (x', y', z') is defined by only two parameters, α and β, to first order in the Euler angles:

$x'=x-\alpha y$; $y'=\alpha x+y-\beta z$; $z'=\beta y+z$.

Differentiating the relations that give the horizontal coordinates as a function of the equatorial coordinates, we obtain

$\Delta az=\alpha-\beta$tan(alt)cos(az) and $\Delta alt=\beta$sin(az),

suggesting α~1.0^o and β~1.1^o. Here α measures a rotation about vertical and β measures the tilt with respect to vertical.

A detailed evaluation of the uncertainties attached to the measurement of the horizontal coordinates of a star requires a preliminary correction for such a tilt and is beyond the

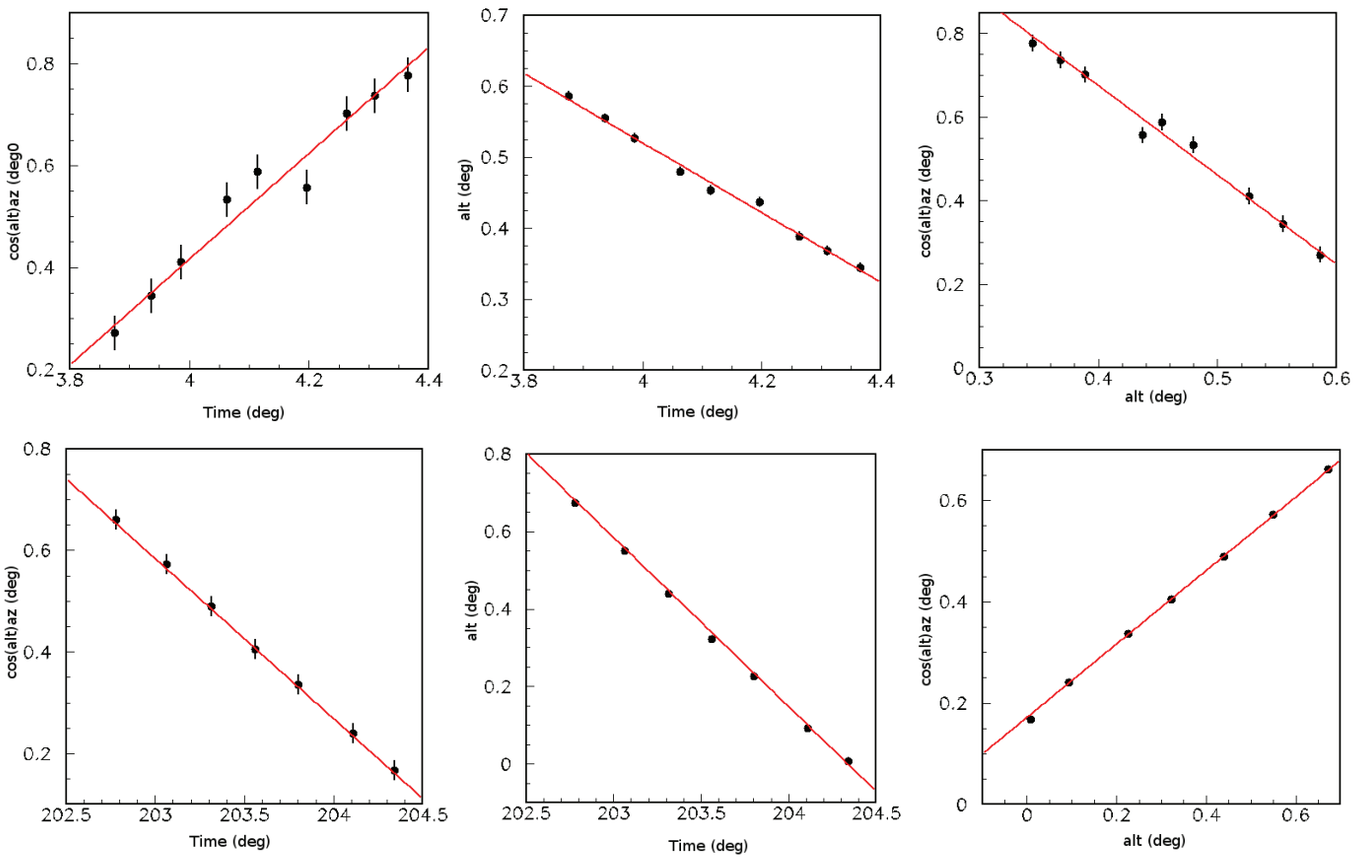

Fig. 16. Dependence of cos(*alt*)*az* (left) and *alt* (middle) over time. Right: dependence of cos(*alt*)*az* over *alt*. Both time and horizontal coordinates are measured in degrees. The upper panels are for observations of φ Aqr made on 17 December 2018 and the lower panels for observations made of Merak (β Ursae Majoris) on 17 May 2019.

scope of the present article. Assuming that the time elapsed since the construction of the observatory is sufficient for the building to have settled to a precision better than a tenth of a degree, it would be advisable to fine-adjust the orientation of the telescope mount to correct for the tilt. Pointing errors are expected at the level of ±5 arcsec~10 px. Ultimately, one should be able to reach precisions of this order of magnitude when measuring the horizontal coordinates of the target. However, this will require more detailed analyses than performed in the present introductory presentation.

Another illustration of the dispersion of successive measurements is displayed in Fig. 16 using observations of φ Aqr made on 17 December 2018 and observations of β Ursae Majoris (Merak) made on 17 May 2019 (Julian date *JD=2458620.5*). Average horizontal coordinates of the telescope pointing were (*az, alt*)=(210.9^0, 59.2^0) for the former and (331.2^0, 45.0^0) for the latter. Linear fits to the dependence on time of the star offsets measured in the CCD array after correction for the different pointing directions provide evaluations of the quantities cos(*alt*)*daz/dt*, *dalt/dt* and cos(*alt*)*daz/dalt* listed in Table 6 together with their true values and the standard deviations of the measurements with respect to the linear fits. Within the uncertainties induced by the tilted geometry, reasonable agreement between the measured and true values of the measured quantities is observed. The values of the standard deviations, particularly small in the case of Merak, confirm the conclusions that were obtained from the analysis of the data listed in Table 4.

Table 6. Movements of φ Aqr and β Ursae Majoris as observed on 17 December 2018 and 17 May 2019, respectively.

	φ Aqr			Merak		
	cos(alt) daz/dt	*dalt/dt*	*cos(alt) daz/dalt*	*cos(alt) daz/dt*	*dalt/dt*	*cos(alt) daz/dalt*
Measured values	1.04	-0.49	-2.14	-0.31	-0.44	0.73
True values	1.12	-0.48	-2.46	-0.32	-0.45	0.72
Standard deviations	0.034	0.007	0.020	0.006	0.009	0.001

4. Conclusions

The exploratory and introductory measurements that have been performed over the past year and that are described

in the present article have demonstrated the high quality of the Hoa Lac observatory telescope as a scientific instrument of outstanding potential in terms of training bachelor's and master's degree students. It is now essential to make sure that the important investment that the acquisition of such an instrument represents is made use of as efficiently as possible. In particular, it must be made accessible to those who are most likely to make good use of it, namely university students and amateur astronomers.

Ideally, a scientific instrument should be granted a yearly operation and maintenance budget at the level of a significant percentage, say 5 to 10%, of the initial investment cost. Ideally also, for a proper exploitation of an optical telescope, weather conditions should be such that the fraction of clear nights during which observations can be performed should well exceed 50%. Unfortunately, in the present case, none of these two conditions can be realised. The operation and maintenance budget available for the exploitation of the telescope is negligible and cloud coverage is such that less than 10% of the nights are clear enough to make observations possible [11]. In order to overcome these handicaps, active cooperation with universities and astronomer clubs is mandatory.

The potential of the telescope as a training tool is twofold: it covers the fields of pure instrumentation and of astronomy observations. The present article has given an idea of what the former may include, continuing the exploratory measurements that have been described in order to reach a detailed understanding of the telescope geometry and perform observations of the highest possible quality. In particular, the horizontal coordinates of the orientation of the "*altaz*" rotation axes of the telescope mount need to be accurately measured, together with the precise location of the optical axis and of the CCD array. Detailed properties of the optical system need to be studied. Third party access to the software should be available. Saturation of the CCD array currently prevents taking pictures of bright targets such as the Moon and planets and solutions have to be found to overcome this problem. The pointing accuracy should be optimized. A system or procedure allowing for operation at temperatures below 0^0C without ice formation on the CCD array needs to be implemented.

For what concerns astronomy observations, in addition to collecting pictures of the highest possible quality, a study of bright, short period variable stars is an example of the kind of observations that could be made in the period during which cloud coverage is not too important, typically between October and April. Fig. 17 shows pictures of two nebulae that illustrate the current performance of the telescope optics.

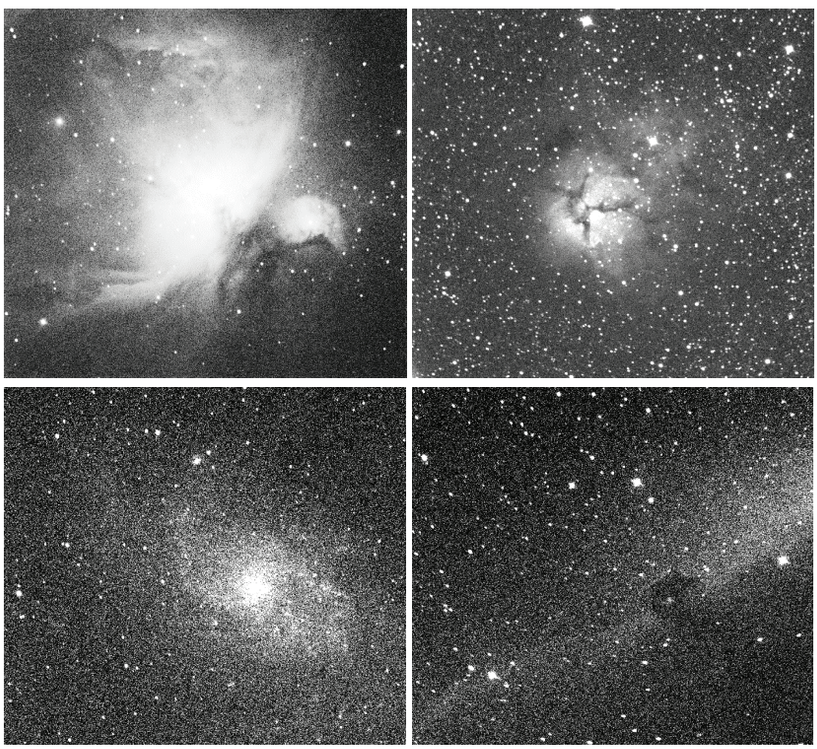

Fig. 17. Up left: picture of the Orion Nebula (100 s exposure time, 19 January 2018). Up right: picture of the Trifid Nebula (30 s exposure time, 19 January 2018). Down left: picture of the Triangulum Galaxy (60 s exposure time, 19 January 2018). Down right: picture of the Horsehead Nebula (60 s exposure time, 4 July 2018).

The research work of the team of the Department of Astrophysics of the Vietnam National Space Center, who is authoring the present article, covers a domain of astronomy and astrophysics essentially disconnected from what the Hoa Lac telescope can access [12]; it uses instruments, such as the Atacama Large Millimeter (submillimeter) Array [13] having sensitivities and angular and spectral resolutions four orders of magnitude larger. Yet, the team will always be available to provide advice and guidance to potential users.

In summary, the opportunity of using the optical telescope of Hoa Lac observatory should not be missed by universities and amateur astronomer clubs. To the former it provides access to a highly performing scientific instrument, with which bachelor and master students can be trained and learn the constraints of rigor and professionalism inherent to the practice of science. To the latter, it offers an opportunity to observe the night sky with one of the best instruments available in the country.

ACKNOWLEDGEMENTS

We thank the anonymous referee for a number of useful comments that helped with improving the quality of the manuscript. We are grateful to the members of the Department of Astrophysics of the Vietnam National Space Center, in particular Dr. Do Thi Hoai, Dr. Pham Thi Tuyet Nhung and Dr. Pham Tuan Anh, for help and useful discussions. This research is funded by the Graduate University of Science and Technology under grant number GUST.STS.NV2017-VL01. Financial support from the Vietnam National Space Center and from the World Laboratory is acknowledged.

The authors declare that there is no conflict of interest regarding the publication of this article.

REFERENCES

[1] http://www.marcontelescopes.com/azienda.php, Marcon-RC500, JEA Technical Solutions Ltd, info@jea-ts.co.uk.

[2] https://www.onsemi.com/pub/Collateral/KAF-16801-D.PDF.

[3] http://www.bisque.com/help/TheSkyXSAEAndPro/index.htm#t=Chart_Navigation.htm.

[4] http://www.astrometric.com/products/telescope-control/.

[5] R. Widenhorn, M. Blouke, A. Weber, A. Rest, and E. Bodegom (2002), "Temperature dependence of dark current in a CCD", *Sensors and camera systems for scientific, industrial, and digital photography application III*, Proceedings of SPIE - The International Society for Optical Engineering, **Vol.4669**, Doi: 10.1117/12.463446

[6] P.N. Dinh, et al. (2003), "Measurement of the Zenith angle distribution of the cosmic muon flux in Hanoi", *Nuclear Physics B*, **661(1-2)**, pp.3-16.

[7] P.N. Dinh, et al. (2002), "Measurement of the vertical cosmic muon flux in a region of large rigidity cutoff", *Nuclear Physics B*, **627(1-2)**, pp.29-42.

[8] M. Wenger, et al. (2000), "The SIMBAD astronomical database. The CDS reference database for astronomical objects", *Astronomy and Astrophysics Supplement*, **143**, pp.9-22.

[9] https://www. maps.google.com/.

[10] O. Montenbruck (1989), *Practical Ephemeris Calculations*, Springer Verlag and http://www.onlineconversion.com/julian_date.htm.

[11] https://weatherspark.com/y/116009/Average-Weather-in-Hanoi-Vietnam-Year-Round.

[12] https://vnsc.org.vn/dap/publications.htm.

[13] https://www.almaobservatory.org/en/home.